Hollow Waveguide Arrays as Quarter- and Half-Wave Plates

Stefan Belle, Stefan F. Helfert, and Ralf Hellmann

***Abstract*—We present hollow waveguide arrays acting like quarter- and half-wave plates. Approximately 2000 × 2500 individual rectangular hollow waveguides filled with air and surrounded by a gold cladding form the basis of the wave plates. The hollow waveguides fabricated by combining femtosecond 3D direct laser writing with electroplating have sub-micron dimensions of less than 500 nm in the cladding area. Both wave plates show the characteristic properties of quarter- and half-wave plates converting a linear polarized input field into a circular (quarter-wave plate) and a linear 180 ° phase shifted polarized output field (half-wave plate). This is confirmed experimentally by measuring the angle-dependent phase shift, the Stokes vectors and polarization ellipses for both wave plates.**

***Index Terms*—Three-dimensional direct laser writing, hollow waveguide array, metallic sub-wavelength structures, quarter- and half-wave plates, polarization optics.**

I. Introduction

POLARIZATION states define a fundamental property of optical radiation and are essential in many areas of both, field industrial applications and scientific research to realize various optical implementations. For example, in optical tweezers the polarization state influences the stability of trapping different nanoparticles in 3-dimensions [1], [2]. The polarization state in laser material processing has a strong influence to the absorption behavior in materials [3], [4]. Further sophisticated applications in which the polarization state is decisive can be found in, e.g., bio imaging [5], [6], acousto-optics [7] or microscopy [8], [9]. In all of these applications, the polarization state is influenced by polarization converters, which transform an optical input beam with a polarization state $\mathcal{P}_1$ into an output polarization state $\mathcal{P}_2$. Any polarization converter is based on an optical anisotropy, its optical properties depending on the propagation direction in the anisotropic material. In natural materials, the molecular structure determines the anisotropy of the material. In artificially manufactured polarization converters, however, only the design or the geometry determines the anisotropy rather than the molecular structure of the material. Known examples of artificially produced polarization elements are dielectric sub-wavelength gratings [10]–[12], photonic crystals [13], [14] and metamaterials [15], [16]. All of the above mentioned artificially fabricated polarization converters have structural dimensions in the sub-wavelength range. Such components with structural dimensions of less than 500 nm require demanding manufacturing methods.

In recent years, additive manufacturing has developed into a versatile manufacturing method in science as well as for a fabrication method in industry. The technology allows for novel 3-dimensional manufacturing of objects directly from a computer-aided design [17]. Among other more exotic technologies, the use of an ultra-short pulse laser enables additive manufacturing to be transferred into the sub-micrometer range [18]. Multiphoton lithography or also known as 3-dimensional direct laser writing (3D DLW) uses a multiphoton absorption excited by tightly focus a beam of an ultra-short pulse laser into the volume of a transparent photosensitive material (photoresist). By moving the beam focus in 3-dimensions inside the photosensitive material, complex 3D structures can be fabricated in a pinpoint writing process [19], [20]. Structures with a line width of less than 100 nm were shown in the past with 3D DLW [21]–[23]. Beside high lateral resolution also the versatile usage in a variety of scientific areas has already been shown, such as biology [24], [25], life sciences [26], [27] and optics [28], [29]. 3D direct laser writing can also be combined with other manufacturing methods in order to add further functionalities to the components produced or to enable their functionality [30]–[32].

II. Polarization Conversion and Polarization Rotation

A. Basic Theory of a Hollow Waveguide

In contrast to the previously presented approaches transforming the polarization from one state into another polarization state, here we follow a different approach predicated on the theoretical work of Helfert *et al.* [33], [34]. The approach used in this work is based on polarization conversion using hollow waveguides. Fig. 1 shows a schematic drawing of a single hollow waveguide element. The hollow waveguide has an air-filled rectangular cross section and the surrounding sidewalls are made of a metal, in this work gold is used. An incident field propagates through the air-filled hollow waveguide and the gold sidewalls act as a mirror. The sidewalls have a high reflectivity and guide the incident field through the hollow waveguide. The birefringence is generated in this component purely geometrically. The two

Manuscript received December 15, 2021; revised March 9, 2022; accepted March 16, 2022. Date of publication March 22, 2022; date of current version April 5, 2022. *(Corresponding author: Stefan Belle.)*

Stefan Belle and Ralf Hellmann are with the Applied Laser and Photonics Group, Aschaffenburg University of Applied Siences, 63743 Aschaffenburg, Germany (e-mail: stefan.belle@th-ab.de; ralf.hellmann@th-ab.de).

Stefan F. Helfert is with the Chair of Micro- and Nanophotonics, FernUniversitaet in Hagen, 58097 Hagen, Germany (e-mail: stefan.helfert@fernuni-hagen.de).

Digital Object Identifier 10.1109/JPHOT.2022.3160878

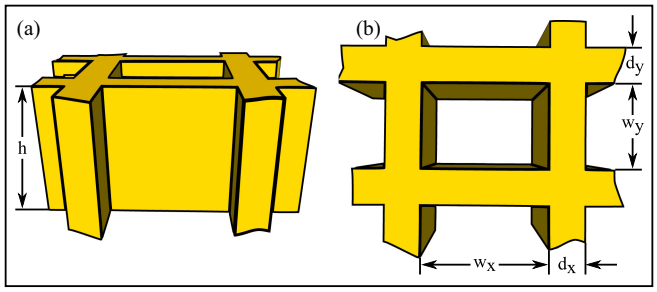

Fig. 1. Schematic drawing of a single hollow waveguide element. Fig. 1(a)) shows a side view and Fig. 1(b)) a top view of one hollow waveguide. The yellow-colored structure are the surrounding gold sidewalls. The bright area in between is the air-filled hollow waveguide.

lowest eigenmodes (TE10 horizontal eigenmode and TE01 vertical eigenmode) have different propagation constants and associated different effective refractive indices. For an ideal metal and a rectangular cross section, (1)–(2) describe the effective refractive indices for the horizontal and vertical propagation constant [33]

$$n_{eff1,0} = \sqrt{1 - \frac{\lambda_0^2}{4w_x^2}} \tag{1}$$

$$n_{eff0,1} = \sqrt{1 - \frac{\lambda_0^2}{4w_y^2}}. \tag{2}$$

In (1)–(2), λ_0 is the free space wavelength and $w_{x,y}$ the dimensions of the horizontal and vertical opening of the hollow waveguide. Apparently, the effective refractive indices and therefore the polarization conversion depends purely on the geometry of the hollow waveguide. Thus, by choosing appropriate dimensions $w_{x,y}$ and height h the desired phase difference

$$\Delta\Phi = k_0(n_{eff1,0} - n_{eff0,1})h \tag{3}$$

can be engineered.

B. Stokes Parameters and Mueller Calculus

The relations derived in this section describe the measured polarization shift shown in Figs. 6 and 7 for both the quarter- and the half-wave plate. To explain the measurement results shown in Section IV, the Stokes parameters are calculated for the light passing the hollow waveguide array and the analyzer. The Stokes parameters S_0, S_1, S_2 & S_3 completely describe the polarization state of light. Parameter S_0 is the total intensity of the light, the parameters S_1 and S_2 express the tendency towards linear polarization ($S_1 = 1$ for horizontal polarization, $S_1 = -1$ for vertical polarization, $S_2 = 1$ for 45 ° linearly polarized light and $S_2 = -1$ for -45 ° linearly polarized light). Parameter S_3 indicates the tendency towards circular polarization ($S_3 = 1$ for left circularly polarized light and $S_3 = -1$ for right circularly polarized light). For the calculation as well as for the measurements, the input beam is horizontal linear polarized. An incident polarized beam S_{in} interacts with polarizing optical elements, and the emerging beam is characterized by a new Stokes column S_{out}. The polarizing optical elements can be described by a $4x4$ matrix which is characteristic of the used devices and known as the Mueller matrix. To calculate the Stokes column of the emerging beam S_{out}, all optical elements, both HWA waveplates and the analyzer, must be indicated with their characteristic matrices [35]. Multiplying the Mueller matrices with S_{in} results in the emerging Stokes column S_{out}:

$$S_{out} = M_{\lambda/4;\lambda/2} M_{pol} S_{in} \tag{4}$$

To calculate the Stokes column of the emerging beam over a full rotation, from 0 ° to 360 °, matrices with variable angles of the HWA and the analyzer are necessary. Both angles are shown in the measurement setup in Fig. 3, α is the rotation angle of the hollow waveguide array and γ the rotation angle of the polarizer/analyzer. The rotation-dependent shift of the maximum or minimum of the intensity caused by rotating the HWA by a value of $\Delta\alpha$ can be calculated using the Stokes parameter S_0 from the Stokes column S_{out}. As the analyzer is rotated, γ is altered and so the Stokes parameter S_0, which is equivalent to the intensity of the transmitted beam. By differentiating S_0 with respect to γ, the maximum or minimum of the intensity occur whenever $dS_0/d\gamma = dI/d\gamma = 0$. This results for a quarter-wave plate in:

$$\frac{dS_0}{d\gamma} = \frac{dI}{d\gamma} = \frac{1}{2} \cdot (-\cos^2 2\alpha \cdot 2\sin 2\gamma + \\ + \cos 2\alpha \cdot \sin 2\alpha \cdot 2\cos 2\gamma) = 0 \tag{5}$$

By simplifying (5), the rotation-dependent shift of the maximum or minimum of the intensity occur at:

$$\gamma = \Delta\alpha \tag{6}$$

Thus, rotating the HWA (quarter-wave plate) by an angle $\Delta\alpha$ causes a rotation-dependent shift of the angle γ by the same value. The rotation of a half-wave plate leads to a different result. Differentiating S_0 with respect to γ results in:

$$\frac{dS_0}{d\gamma} = \frac{dI}{d\gamma} = \frac{1}{2} \cdot (-\cos 4\alpha \cdot 2\sin 2\gamma + \\ + \sin 4\alpha \cdot 2\cos 2\gamma) = 0 \tag{7}$$

Here, by simplifying (7) the angle-depended shift of the maximum or minimum occur at:

$$\gamma = 2\Delta\alpha \tag{8}$$

Summarizing (8), a rotation-dependent shift of the maximum or minimum of the intensity by the angle γ is caused by rotating the hollow waveguide array (half-wave plate) by an amount twice of γ. The resulting rotation-dependent polarization is examined in detail in Section IV-A when discussing the measurement results.

III. Fabrication

The polarization converter is based on the concept of hollow waveguides, as they are also known from in microwave technology [36]. A rectangular hollow waveguide consists of a dielectric medium surrounded by a metallic cladding. The anisotropy of propagation constants and therefore a phase shift between the horizontal and vertical field components is achieved by the

rectangular geometry of the hollow waveguide. The geometry of the hollow waveguide array (HWA) is mainly defined by the structure height. With a height of the photoresist pillars of ≥ 3 μm, the pillars tend to stick together due to the small distance between them. In order to avoid overgrowth during the electrochemical deposition, the height of the freestanding pillars should be about 1.4 times higher than the deposited height. Both, the maximum height of the pillars and the factor to avoid overgrowing results to a final height of the HWA of 2 μm. The remaining geometry w_x and w_y of a hollow waveguide can be calculated with (1)–(3).

The complete fabrication of a hollow waveguide array can be divided into two sub-processes. First, the fabrication of a negative structure of the HWA. For this process step, an adhesion promotor TiPrime (MicroChemicals GmbH, Germany) is spin coated onto a cleaned indium tin oxide (ITO) coated quartz glass substrate (Zeiss AG, Germany). The rotational speed for this process step is 3000 rpm and the adhesion promotor is activated in a subsequent baking step at 120 °C for 2 min. Subsequently, the positive tone photoresist AZ3027 (MicroChemicals GmbH, Germany) is applied by spin coating with a rotational speed of 2800 rpm. For mechanical and chemical stabilization of the spin coated layer, the sample is baked on a hotplate at 100 °C to reduce the solvent content of the photoresist. Following, the photoresist is exposed with a 3D LDW-setup Photonic Professional GT (Nanoscribe GmbH, Germany). The average laser power behind the microscope objective, with a numerical aperture of NA = 1.4, is 12.5 mW and the writing speed is 15 mm/s. Using a microscope objective with a high numerical aperture results in generating exposed areas with a width of about 200 nm and height of about 800 nm. For this the polymerized focal volume (voxel) is not large enough for an exposure of the entire height of the photoresist. Therefore, the photoresist must be exposed several times in different levels. One writing field has an area of 100 μm x 100 μm and the writing fields are stitched together to get the entire array with a total area of about 4 mm x 4 mm. Immediately after exposure, the resist film is baked at 110 °C for 1 min and developed in a ready to use developer AZ726MIF (MicroChemicals GmbH, Germany) for 1 min. The developed photoresist layer is thoroughly rinsed with deionized water. The resulting freestanding photoresist pillars are shown in Fig. 2(a)).

In the second sub-process, gold is electrochemically deposited into the dissolved areas. For this sub-process, the ITO coated glass substrate with the freestanding photoresist pillars is built into an electrochemical deposition chamber and is placed onto a heating plate at 60 °C. To achieve a smooth cladding surface and a good mechanical stability, the electrochemical deposition is performed by alternating pulsed and constant current. The total time for electrochemical deposition is about 18 min, resulting in a gold height of 2 μm. In order to enhance the adhesion of the gold layer on top of the ITO, a EpoCore5 negative tone photoresist (MicroResist GmbH, Germany) is spin coated with a rotational speed of 3000 rpm over the entire structure and softbaked at 90 °C for 5 min. Subsequently, the photoresist is exposed by UV-light of a mask aligner EVG620 (EVG GmbH, Austria) at a dose of 220 mJ/cm^2. After exposure, a hardbake is done at 85 °C for 5 min and the sample is developed in a ready to use developer mr-Dev 600 (MicroResist GmbH, Germany) for 50 s. With this last developing step, a circular area of 2 mm in diameter is opened and within this circular area also the freestanding pillars are completely removed by the developer. The final hollow waveguide array is shown in Fig. 2(b)). A more detailed description of the fabrication process can be found in Belle *et al.* [37].

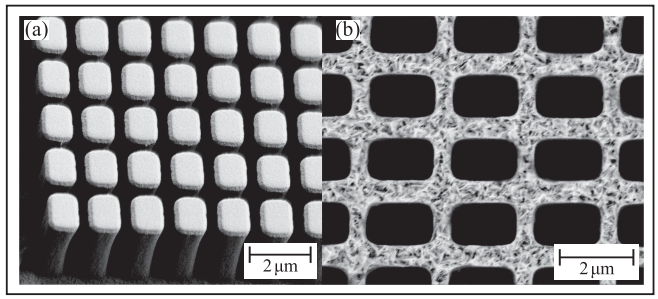

Fig. 2. Scanning electron microscope images of a) freestanding photoresist pillars after the 3D DLW process and development and of b) the final gold structure of the hollow waveguide array.

With the advanced fabrication process presented in this work, the dimensions of the hollow waveguides can be changed in a targeted manner and thus any phase delay can be engineered. Furthermore, it is possible to change the dimension of the geometry down to individual hollow waveguides. With correct parameters for the fabrication and for the geometry of the hollow waveguides are established, the throughput is around 95 %.

IV. Experimental Section

The average height of the HWAs are determined using a Dektak XT tactile surface profilometer (Bruker GmbH, Germany), whereas the waveguide dimensions (w_x & w_y) and the width of the metal side walls (d_x & d_y) are measured using a MAIA3 scanning electron microscope (Tescan GmbH, Germany). The average height h is determined at three positions, to the left of the sample center approx. 500 μm from the edge, in the middle of the sample and to the right of the sample center also approx. 500 μm from the edge. The measurements at these points extend over the entire sample and are repeated ten times at each position. Statistical evaluation yields an average height of $h = 1967 \pm 121$ nm. To determine the waveguide geometry, a total of 25 waveguides are measured at random positions over the entire HWA. For the quarter-wave plate, the dimensions of the hollow waveguides are $w_x = 1551 \pm 4$ nm and $w_y = 1034 \pm 3$ nm. The half-wave plate has the same dimension $w_x = 1550 \pm 5$ nm in the x-direction as the quarter-wave plate. Only in the y-direction $\mathrm{w_y} = 870 \pm 4$ nm both polarization converters differ. For both polarization converters, the dimensions of the metal sidewalls are $d_x = 396 \pm 6$ nm and $d_y = 421 \pm 7$ nm. The waveguide geometries from the fabricated HWA show excellent agreement with the targeted values of $w_x = 1550$ nm and $w_y = 1034$ nm (quarter-wave plate) as well as $w_x = 1550$ nm and $w_y = 872$ nm (half-wave plate) at a height of $h = 2000$ nm. The width of the metal sidewalls, however, does not influence the polarization behavior of the polarization converters, only the transmission

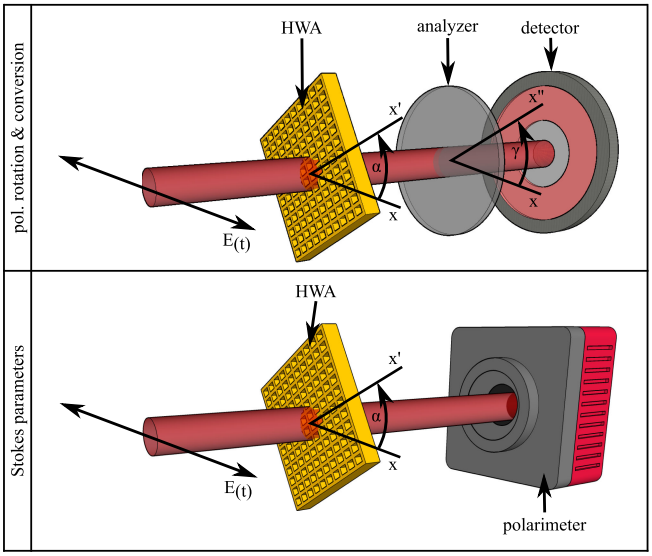

Fig. 3. Setup for measuring polarization degree and polarization rotation (top) and setup for measuring the Stokes parameter and the polarization ellipse (bottom). The input laser beam is polarized horizontally.

depends on the width of the sidewalls. While the transmission of the quarter-wave plate is 62.3 ± 0.18 %, the transmission of the half-wave plate amounts to 56.8 ± 0.13 %. This difference can be assigned by the different waveguide dimensions of $w_{y,\lambda/4} > w_{y,\lambda/2}$. Due to the smaller waveguide width w_y of the half-wave plate, the proportionate higher amount of metal sidewalls on the same square area reduces the transmission. The reproducibility of different polarization converters is high, the measured geometries are all within the ranges given here.

The setups shown in Fig. 3 are used to characterize the polarization dependent behaviour of the quarter- and half-wave plate. The two setups consist of a laser diode emitting in constant mode at a wavelength of $\lambda = 1550$ nm, a beam collimation and the hollow waveguide (both the laser and the beam collimation are not shown in the top and bottom figure). For the determination of the polarization rotation, the setup is expanded with a linear polarizer/ analyzer and a detector (see upper figure), for the measurement of the Stokes parameters and the polarization ellipses only a polarimeter PAX1000IR2/M (Thorlabs GmbH, Germany) replaces the analyzer and detector in the setup.

A. *Rotation-Dependent Polarization Shift*

The rotation-dependent polarization shift is theoretically described in Section II-B. Based on the calculation performed with the Mueller calculus, it can be shown that rotating the HWA (quarter-wave plate) by an angle $\Delta\alpha$ shifts the intensity transmitted by the analyzer and thus the polarization at the output by the same amount. By rotating the half-wave plate by an angle $\Delta\alpha$, the polarization at the output shifts twice the value. The polarization shifts and the principle operation of the quarter- and half-wave plate are experimentally demonstrated and quantified in the following. The setup shown in Fig. 3 (top) is used here for the characterization. For the measurements, the angle α of the

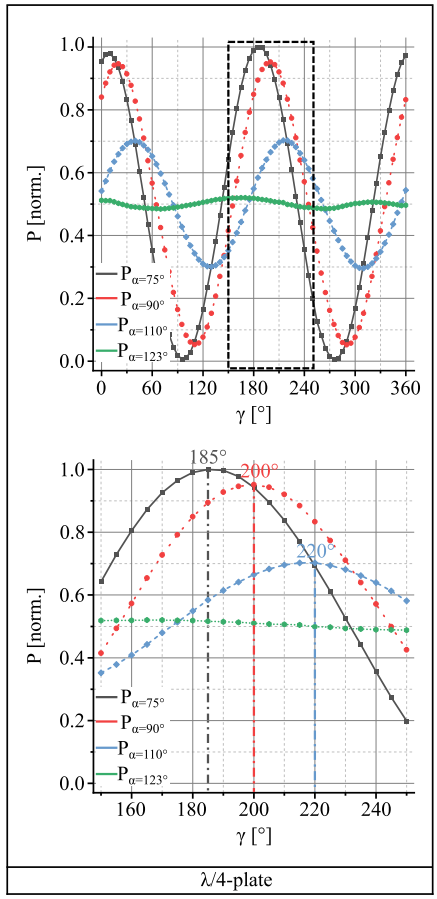

Fig. 4. Normalized transmitted power as a function of the analyzer angle for different angular positions of the HWA operating as a quarter-wave plate. Top, Normalized power over one full rotation of the analyzer and bottom a zoomed view of the rectangular area. Please note that since the measurement errors here are small, no error bars are included in this figure.

hollow waveguide array is set to a fixed value and the angle γ of the analyzer is changed stepwise from 0 ° to 360 ° by increments of 5 ° and the transmitted power is measured for each angle of the analyzer.

Fig. 4 summarizes the results for the quarter- and Fig. 5 for the half-wave plate over the complete angular range from 0 ° to 360 ° of the analyzer (top) and, in addition, a more detailed view at a region of interest (bottom). The angular positions of the quarter wave plate is selected to show linear polarization, circular polarization and two elliptical polarization states. The dark gray line from Fig. 4 (top) shows the typical curve through an analyzer transmitted power of a linearly polarized beam. The field components parallel to the transmission axis of the analyzer correspond to a normalized power value of $P = 1$, the field components perpendicular to the transmission axis of the analyzer are completely blocked and correspond to a power value of $P = 0$. Changing the angular position α of the hollow waveguide array from linear polarization to elliptical polarization, changes also the distribution of the excited field components in the hollow waveguides. For elliptical polarization both modes are excited with different weightings, therefore the

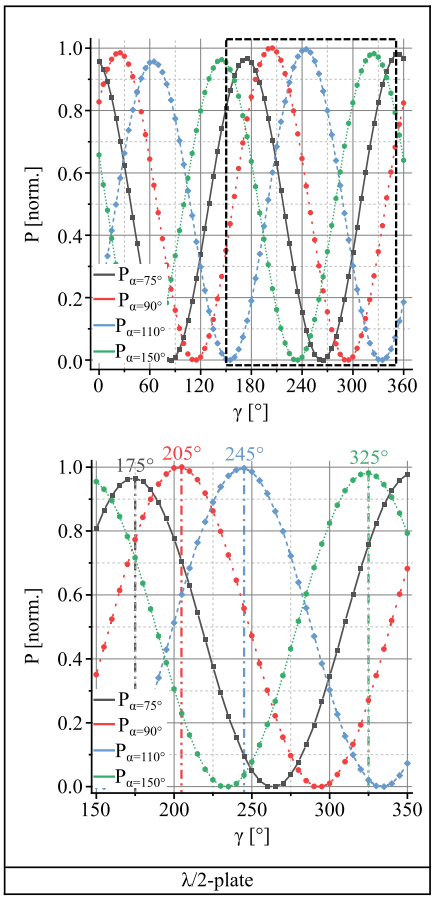

Fig. 5. Normalized transmitted power as a function of the analyzer angle for different angular positions of the HWA operating as a half-wave plate. Top, Normalized power over one full rotation of the analyzer and bottom a zoomed view of the rectangular area. Please note that since the measurement errors here are small, no error bars are included in this figure.

maximum and minimum transmitted power of $P = 1$ and $P = 0$ are not reached and the curves becomes flatter (red and blue curve). Two equally excited field components results in a maximum phase difference of $\Delta\Phi = \pi/2$ and the HWA converts the linear polarization of the input beam into a circular output polarization. Due to the identical field components, there is no preferred direction and the transmitted power corresponds to $P \approx 0.5$ (green curve) over the entire angular range of the analyzer.

The hollow waveguide array as a half-wave plate changes only the direction of polarization. Therefore, a linearly polarized input beam remains linearly polarized at the output and only changes the angle of the polarization direction. Fig. 5 (top) shows the optical power transmitted through the analyzer as a function of a complete analyzer rotation of 360 ° for various positions of the HWA. Independent of the angle position α of the HWA, only one field component is excited and the field component perpendicular to the excited one is blocked by the analyzer. These results are comparable to results from the quarter-wave plate at the angular position $\alpha = 75$ °. In contrast to the HWA acting as a quarter-wave plate, however, the intensity curves does not change its profile because the output field remains linearly polarized for every position of the hollow waveguide array.

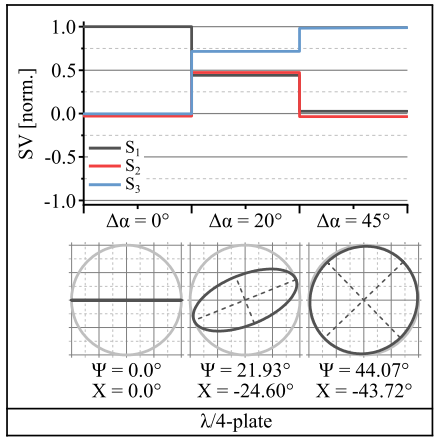

Fig. 6. Normalized Stokes parameters of a quarter-wave plate and the corresponding polarization ellipse.

The diagrams at the bottom of Figs. 4 and 5 show a zoomed section of the above diagrams, as indicated by a dashed rectangular area. For the quarter-wave plate it can be clearly seen, that the maximum positions of the transmitted power changes by the same value as the rotated angle $\Delta\alpha$ of HWA. If the HWA is rotated by 15 °, the position of the maximum also rotates by 15 ° (dark gray to red curve, in the bottom of Fig. 4). For a further changing from 90 ° to 110 ° of the HWA (red to blue curve), there is also a polarization rotation of the same value. For a half-wave plate the polarisation rotation is different, here the rotation angle doubles. By changing the angular position of the HWA comparable to the quarter wave plate by 15 °, the direction of the output polarization rotates by 30 ° (gray to red curve, in the bottom of Fig. 5). For a further changing from 90 ° to 110 ° of the HWA, the polarization direction rotates accordingly by 40 ° (red to blue curve). This corresponds exactly to the calculated values from Section II-B for the polarization shift of a quarter- and half-wave plate ((6) and (8)).

Smaller deviations of the measured values from theoretical values can be explained by the spectral width of the laser diode of $\Delta\lambda = 4$ nm at the full width at half maximum, the slight deviation from the targeted dimensions of the hollow waveguides and a slight rounding of the hollow waveguides through the fabrication process, as can be seen in Fig. 2. This rounding occurs during the exposure by 3D DLW, in which all lines are exposed in x-direction first and secondly in y-direction over the entire writing field. The crossing of the lines in x- and y-direction are therefore double exposed. Due to the higher energy input, there is a slight diffusion of photo acids and the corners are rounded [38]. Therefore, the cross section of the waveguide do not exactly match with the actual dimensions of the fabricated hollow waveguides. In this case, the two eigenmodes are not exactly orthogonal in their polarization and a deviation appears at the sides and corners of the HWA.

B. Stokes Vectors

In addition to the previous measurement, the measurement of rotation-dependent polarization shift, the polarization conversion of the two waveplates is to be confirmed by a polarimeter.

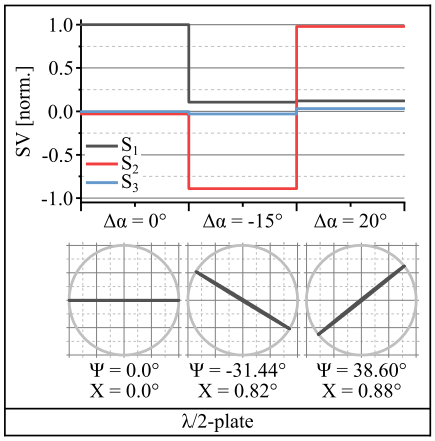

Fig. 7. Normalized Stokes parameters of a half-wave plate and the corresponding polarization ellipse.

The setup shown in Fig. 3 (bottom) is used for this measurement. In the setup the analyzer and detector are replaced by a polarimeter. Both hollow waveguide arrays are measured for different angular positions and the results are shown in Fig. 6 for the quarter-wave plate and in Fig. 7 for the half-wave plate.

As described in Section II-B, the Stokes vectors S_0, S_1, S_2 & S_3 completely describe the polarization state of light. While the parameter S_0 corresponds to the total intensity of the light, the parameters S_1, S_2 & S_3 describe the polarization state. For a beam that is completely polarized $S_0^2 = S_1^2 + S_2^2 + S_3^2$. In the measurements the total intensity is normalized to 1, thus S_1, S_2 & S_3 can have values between -1 and 1. For both measurements, the input beam is horizontal linear polarized. The Stokes vectors for horizontal linear polarized light are $S_1 = 1$ and $S_2 = S_3 = 0$. The polarization ellipse below the Stokes vectors shows also this orientation, the azimuth $\Psi = 0\,^\circ$ and the ellipticity $\chi = 0\,^\circ$ corresponding for a linear horizontal polarization. If the quarter-wave plate is rotated from linear to elliptical polarization, the Stokes vectors change accordingly, S_1 becomes less than 1, S_2 increases due to the polarization rotation and S_3 also increases because the circular weighting increases. For the polarization ellipses, the azimuth changes according to the angular rotation $\Delta\alpha$ by the same value and the ellipticity increases because of exciting both field components in x- and y-direction. By rotating the HWA further to the maximum phase difference of $\Delta\Phi = \pi/2$, the two Stokes vectors S_1 & S_2 become 0, because these only describe the linear polarization, and S_3 increase to 1 for left circularly polarized light. The ellipticity of the polarization ellipse is at its maximum and the azimuth angle, again, rotates at the same value as the rotating angle α of the HWA, like calculated in (6).

For the half-wave plate shown in Fig. 7, the Stokes vector $S_3 = 0$ does not change over the entire measurement. Because the half-wave plate does not change the polarization state, only the polarization direction is changed and the output field remains linearly polarized. For this S_1 becomes close to 0 and S_2 changes according to the diagonal direction of polarization from $S_2 = 0$ at the input to $S_2 = $ -0.83 by changing the direction of polarization by $-15\,^\circ$. A further changing of the polarization direction from $-15\,^\circ$ to $20\,^\circ$ leads to a value of $S_2 \approx 1$. Due to the linear polarization, the ellipticity remains constant at $0\,^\circ$, only the position of the azimuth changes twice to the rotation of the HWA, as calculated in (8). Except of small deviations of the measurement values from the optimum values, all results clearly highlight the possibilities of the hollow waveguide array as to be used as a quarter- and half-wave plate.

V. Conclusion

We have shown full functional operability of a hollow waveguide array, fabricated by femtosecond direct laser writing, as quarter- and half-wave plates for optical radiation at 1550 nm. The polarization conversion of these wave plates is based on the geometric conditions of a hollow waveguide array. Through measurements of the polarization shift, the Stokes vectors and the polarization ellipse it is demonstrated that the polarization converters exhibit, in general, the predicted properties comparable to commercially available quarter- and half-wave plates. The approach pursued here, spotlights the possibility of manipulating polarization states.

Disclosures

The authors declare no conflicts of interest.

Data availability

Data underlying the results presented in this paper are not publicly available at this time but may be obtained from the authors upon reasonable request.

References

[1] G. Cipparrone, I. Ricardez-Vargas, P. Pagliusi, and C. Provenzano, "polarization gradient: Exploring an original route for optical trapping and manipulation," *Opt. Exp.*, vol. 18, no. 6, pp. 6008–6013, 2010.
[2] A. Usman, W.-Y. Chiang, and H. Masuhara, "Optical trapping and polarization-controlled scattering of dielectric spherical nanoparticles by femtosecond laser pulses," *J. Photochemistry Photobiol. A: Chem.*, vol. 234, pp. 83–90, 2012.
[3] M. Meier, V. Romano, and T. Feurer, "Material processing with pulsed radially and azimuthally polarized laser radiation," *Appl. Phys. A*, vol. 86, no. 3, pp. 329–334, 2007.
[4] A. Patel, V. T. Tikhonchuk, J. Zhang, and P. G. Kazansky, "Non-paraxial polarization spatio-temporal coupling in ultrafast laser material processing," *Laser Photon. Rev.*, vol. 11, no. 3, 2017, Art. no. 1600290.
[5] G. Kwiatkowski, F. Jöhnig, J. Steinhauser, P. Wespi, M. Ernst, and S. Kozerke, "Direct hyperpolarization of micro- and nanodiamonds for bioimaging applications - considerations on particle size, functionalization and polarization loss," *J. Magn. Reson.*, vol. 286, pp. 42–51, 2018.
[6] C. Ding, C. Li, F. Deng, and G. J. Simpson, "Axially-offset differential interference contrast microscopy via polarization wavefront shaping," *Opt. Exp.*, vol. 27, no. 4, pp. 3837–3850, 2019.
[7] K. Ishikawa *et al.*, "Optical sensing of sound fields: Non-contact, quantitative, and single-shot imaging of sound using high-speed polarization camera," in *Proc. Meetings Acoust.*, vol. 29, no. 030005, 2016, pp. 1–8.
[8] A. S. Backer, A. S. Biebricher, G. A. King, G. J. L. Wuite, I. Heller, and E. J. G. Peterman, "Single-molecule polarization microscopy of dna intercalators sheds light on the structure of s-dna," *Sci. Adv.*, vol. 5, no. 3, 2019, Art. no. 1083.
[9] J. Morizet *et al.*, "High-speed polarization-resolved third-harmonic microscopy," *Optica*, vol. 6, no. 3, pp. 385–388, 2019.
[10] Z. Bomzon, G. Biener, V. Kleiner, and E. Hasman, "Radially and azimuthally polarized beams generated by space-variant dielectric subwavelength gratings," *Opt. Lett.*, vol. 27, no. 5, pp. 285–287, 2002.

[11] T. Kümpfe and O. Parriaux, "Depth-minimized, large period half-wave corrugation for linear to radial and azimuthal polarization transformation by grating-mode phase management," *J. Opt. Soc. Amer. A., Opt., Image Science, Vis.*, vol. 28, no. 11, pp. 2235–2242, 2011.
[12] Z. Ghadyani *et al.*, "Concentric ring metal grating for generating radially polarized light," *Appl. Opt.*, vol. 50, no. 16, pp. 2451–2457, 2011.
[13] Y. Hu *et al.*, "Toward direct laser writing of actively tuneable 3D photonic crystals," *Adv. Opt. Mater.*, vol. 5, 2017, Art. no. 1600458.
[14] Y. Li, D. B. Fullager, D. Childers, R. Fesperman, G. Boreman, and T. Hofmann, "High-contrast infrared polymer photonic crystals fabricated by direct laser writing," *Opt. Lett.*, vol. 43, no. 19, pp. 4711–4714, 2018.
[15] L. Cong *et al.*, "A perfect metamaterial polarization rotator," *Appl. Phys. Lett.*, vol. 103, no. 17, 2013, Art. no. 171107.
[16] J. Xu, R. Li, S. Wang, and T. Han, "Ultra-broadband linear polarization converter based on anisotropic metasurface," *Opt. Exp.*, vol. 26, no. 20, pp. 26235–26241, 2018.
[17] M. Vaezi, H. Seitz, and S. Yang, "Erratum to: A review on 3D micro-additive manufacturing technologies," *Int. J. Adv. Manuf. Technol.*, vol. 67, no. 5-8, 2013, Art. no. 1957.
[18] M. Thiel, J. Fischer, G. von Freymann, and M. Wegener, "Direct laser writing of three-dimensional submicron structures using a continuous-wave laser at," *Appl. Phys. Lett.*, vol. 97, 2010, Art. no. 221102.
[19] M. Malinauskas, M. Farsari, A. Piskarskas, and S. Juodkazis, "Ultrafast laser nanostructuring of photopolymers: A decade of advances," *Phys. Rep.*, vol. 533, no. 1, pp. 1–31, 2013.
[20] L. Jonušauskas *et al.*, "Optically clear and resilient free-form -optics 3D-printed via ultrafast laser lithography," *Materials*, vol. 10, no. 1, pp. 12:1–12:18, 2017.
[21] J. Fischer and M. Wegener, "Three-dimensional optical laser lithography beyond the diffraction limit," *Laser Photon. Rev.*, vol. 7, no. 1, pp. 22–44, 2013.
[22] Z. Gan, Y. Cao, R. A. Evans, and M. Gu, "Three-dimensional deep sub-diffraction optical beam lithography with 9 nm feature size," *Nature Commun.*, vol. 4, 2013, Art. no. 2061.
[23] S. Rekštyté *et al.*, "Nanoscale precision of 3D polymerization via polarization control," *Adv. Opt. Mater.*, vol. 4, no. 8, pp. 1209–1214, 2016.
[24] A. Trautmann, M. Rüth, H.-D. Lemke, T. Walther, and R. Hellmann, "Two-photon polymerization based large scaffolds for adhesion and proliferation studies of human primary fibroblasts," *Opt. Laser Technol.*, vol. 106, pp. 474–480, 2018.
[25] J. Song, C. Michas, C. S. Chen, A. E. White, and M. W. Grinstaff, "From simple to architecturally complex hydrogel scaffolds for cell and tissue engineering applications: Opportunities presented by two-photon polymerization," *Adv. Healthcare Mater.*, vol. 9, no. 1, 2020, Art. no. e1901217.
[26] A. Trautmann, B. Götzendorfer, T. Walther, and R. Hellmann, "Scaffolds in a shell-a new approach combining one-photon and two-photon polymerization," *Opt. Exp.*, vol. 26, no. 23, pp. 29659–29668, 2018.
[27] A. Trautmann, G.-L. Roth, B. Nujiqi, T. Walther, and R. Hellmann, "Towards a versatile point-of-care system combining femtosecond laser generated microfluidic channels and direct laser written microneedle arrays," *Microsystems Nanoeng.*, vol. 5, no. 6, pp. 1–9, 2019, Art. no. 6.
[28] T. Gissibl, S. Thiele, A. Herkommer, and H. Giessen, "Two-photon direct laser writing of ultracompact multi-lens objectives," *Nature Photon.*, vol. 10, no. 8, pp. 554–560, 2016.
[29] S. Yu, H. Zuo, X. Sun, J. Liu, T. Gu, and J. Hu, "Optical free-form couplers for high-density integrated photonics (offchip): A universal optical interface," *J. Lightw. Technol.*, vol. 38, no. 13, pp. 3358–3365, Jul. 2020.
[30] Y. Lin and J. Xu, "Microstructures fabricated by two-photon polymerization and their remote manipulation techniques: Toward 3D printing of micromachines," *Adv. Opt. Mater.*, vol. 6, no. 8, 2018, Art. no. 1701359.
[31] S. Puce *et al.*, "3D-microfabrication by two-photon polymerization of an integrated sacrificial stencil mask," *Micro Nano Eng.*, vol. 2, pp. 70–75, 2019.
[32] P. R. Miller *et al.*, "Fabrication of hollow metal microneedle arrays using a molding and electroplating method," *MRS Adv.*, vol. 4, no. 24, pp. 1417–1426, 2019.
[33] S. F. Helfert, A. Edelmann, and J. Jahns, "Hollow waveguides as polarization converting elements: A theoretical study," *J. Eur. Opt. Society: Rapid Pub.*, vol. 10, pp. 15006:1–15006:7, 2015.
[34] S. F. Helfert, T. Seiler, J. Jahns, J. Becker, P. Jakobs, and A. Bacher, "Numerical simulation of hollow waveguide arrays as polarization converting elements and experimental verification," *Opt. Quantum Electron.*, vol. 49, no. 9, pp. 313:1–131:15, 2017.
[35] A. Gerrard and J. M. Burch, *Introduction to Matrix Methods in Optics.* New York, NY, USA: Dover, 1994.
[36] R. E. Collin and H. Chang, "Field theory of guided waves," *Phys. Today*, vol. 14, no. 9, pp. 50–51, 1961.
[37] S. Belle, B. Goetzendorfer, and R. Hellmann, "Challenges in a hybrid fabrication process to generate metallic polarization elements with sub-wavelength dimensions," *Materials*, vol. 13, no. 22, pp. 5279:1–5279:14, 2020, Art. no. 5279.
[38] E. H. Hall and G. von Freymann, "Spatio-temporal proximity characteristics in 3D μ-printing via multi-photon absorption," *Polymers*, vol. 8, no. 8, pp. 297:1–297:13, 2016.